The Astrophysical Journal, 637:880–888, 2006 February 1

A SEARCH FOR EARLY OPTICAL EMISSION AT GAMMA-RAY BURST LOCATIONS BY THE *SOLAR MASS EJECTION IMAGER* (*SMEI*)

Andrew Buffington,[1] David L. Band,[2,3] Bernard V. Jackson,[1] P. Paul Hick,[1] and Aaron C. Smith[1]

Received 2005 August 2; accepted 2005 September 27

ABSTRACT

The *Solar Mass Ejection Imager* (*SMEI*) views nearly every point on the sky once every 102 minutes and can detect point sources as faint as $R \sim 10$ mag. Therefore, *SMEI* can detect or provide upper limits for the optical afterglow from gamma-ray bursts in the tens of minutes after the burst, when different shocked regions may emit optically. Here we provide upper limits for 58 bursts between 2003 February and 2005 April.

Subject headings: gamma rays: bursts — techniques: photometric

1. INTRODUCTION

Optical emission during and immediately after a gamma-ray burst (GRB) may probe crucial physical processes in the evolution of these bursts, but until recently it has been poorly observed. Therefore, every additional detection and upper limit during this period is relevant to the physical understanding of the burst phenomenon. Here we report on the observations provided by the *Solar Mass Ejection Imager* (*SMEI*), a wide-angle optical telescope launched into low-Earth orbit in February, 2003. *SMEI* scans nearly the entire sky every orbit, viewing each sidereal location for approximately 1 minute with a 102 minute cadence. Thus, *SMEI* can provide a photometric measurement at the location of a gamma-ray burster within 51 minutes of the burst itself.

GRBs are thought to result from a relativistic jet pointed toward Earth, following the release of more than 10^{51} ergs in sources at cosmological distances. The flow in the jet is optically thick initially, thus concealing details of the progenitor (see Piran 2005 and references therein for details of the physical model). The gamma rays are thought to originate in "internal shocks" in this flow (Fenimore et al. 1996); except in the perhaps unusual case in which the flow is uniform, regions having different Lorentz factors collide. These internal shocks may also radiate in the optical. The flow propagates out to the surrounding medium, which may be either an interstellar medium (ISM) unperturbed by the progenitor, or a circumstellar medium (CSM) produced by the progenitor, resulting in the "external shock." The X-ray through radio afterglow following the gamma-ray phase is attributed to synchrotron emission in the external shock (Mészáros & Rees 1997). Afterglows observed from hours to months after the burst (van Paradijs et al. 2000) are modeled by a simple relativistic blast wave. However, before the self-similar blast wave phase (the relativistic analog of the Sedov-Taylor blast wave), the interaction between the flow generating gamma-rays and the surrounding medium is characterized by a forward shock propagating into the surrounding medium and a reverse shock propagating into the burst's relativistic flow (Nakar & Piran 2004). The Lorentz factors and magnetic fields differ in these shocks, resulting in different predictions of the possible optical emission.

Thus, we may observe optical emission from

1. internal shocks during the burst,
2. either the reverse or forward shock at the end of the burst, or
3. the external shock propagating into the surrounding medium during the afterglow.

Therefore, optical observations starting during the gamma-ray emission, and continuing until the afterglow is firmly established, probe the burst's evolution from a relativistic flow dominated by internal shocks, through the complex interaction between the flow and the surrounding medium, until a simple blast wave forms. However, obtaining the requisite optical observations during this period requires rapid detection and localization of the burst. This may be done autonomously, as with the *Swift* program (see below), or it may instead be followed by immediate notification of and quick reaction by telescopes at optical observatories. Alternatively, an optical telescope may already be observing the burst location, either serendipitously or by design, using a wide field-of-view (FOV) telescope to monitor the GRB's sky location.

Robotic telescopes such as the Livermore Optical Transient Imaging System (LOTIS; Williams et al. 1999) and the Robotic Optical Transient Search Experiment (ROTSE; Akerlof et al. 2000) provided some of the first detections and upper limits of the optical emission in the minutes after a burst. The first detection of optical emission during a burst was by ROTSE during the burst GRB 990123 (Akerlof et al. 1999). Here the optical light curve increased to $V = 8.9$ and then decreased, and was uncorrelated with the gamma rays (Briggs et al. 1999). Kulkarni et al. (1999) also detected a radio flare a day after this burst, supporting the hypothesis that the optical emission was due to synchrotron emission from the reverse shock.

More recently, optical emission (Vestrand et al. 2005) during, and infrared (Blake et al. 2005) during and immediately after, the burst GRB 041219A was detected. One of the Rapid Telescopes for Optical Response (RAPTOR) began observing the burst a little over 100 s after the burst trigger, which was a precursor 250 s before the burst's main peak. Therefore, RAPTOR followed the optical emission during the burst's brightest emission; the optical emission peaked at an extinction-corrected $R_c \sim 13.7$. Although the RAPTOR observations lacked time resolution, they are consistent with being correlated with the gamma-ray emission, contrary to the optical–gamma-ray relationship

[1] Center for Astrophysics and Space Sciences, University of California, San Diego, CA 92093-0424; abuffington@ucsd.edu, bvjackson@ucsd.edu, pphick@ucsd.edu.

[2] GLAST SSC, Code 661, NASA Goddard Space Flight Center, Greenbelt, MD 20771.

[3] Joint Center for Astrophysics, Physics Department, University of Maryland Baltimore County, 1000 Hilltop Circle, Baltimore, MD 21250; dband@milkyway.gsfc.nasa.gov.

during GRB 990123 (Vestrand et al. 2005). The maximum infrared fluxes ($J \sim 14$, $H \sim 15$, and $K_s \sim 16$) were observed when the Peters Automated Infrared Imaging Telescope (PAIRITEL) slewed to the burst location 400 s after the burst began, while the burst was still in progress. During the following 3000 s the infrared flux varied, suggesting that the light curve peaks 3 times, perhaps resulting from some combination of internal shocks and the forward and reverse shocks from the external shock region (Blake et al. 2005). Based on both the RAPTOR and PAIRITEL observations, Vestrand et al. (2005) suggest that the gamma-ray spectrum extends to optical wavelengths during the burst, the reverse and forward shocks during the afterglow's early phase enhance optical-infrared emission, and the late afterglow results in fading optical emission.

In addition to these two bursts with optical emission during the burst, afterglow emission as bright as 15 mag has also been detected from a number of bursts, e.g., GRB 021211 (Vestrand et al. 2004; Nysewander et al. 2005; Li et al. 2003), GRB 050502A (Yost et al. 2005), GRB 050525A (Rykoff et al. 2005b), and GRB 050801 (Rykoff et al. 2005a).

Launched in 2004 November, the *Swift* observatory (Gehrels et al. 2004) detects and localizes bursts with its Burst Alert Telescope (BAT), a 15–150 keV coded-mask detector, and then slews to place the burst within the FOV of the onboard X-Ray Telescope (XRT) and UV-Optical Telescope (UVOT), which are co-aligned with the center of the BAT's much larger FOV. Thus, the UVOT on *Swift* should observe early optical emission from a large number of GRBs. However, because of operational constraints, the UVOT will not always be able to observe each burst that *Swift* detects within the first few minutes of the burst, nor will *Swift* detect every burst in the sky.

SMEI (see § 2) is a spaceborne optical monitor having a FOV of $3^\circ \times 160^\circ$ that scans over nearly the entire sky every orbit. *SMEI*'s primary objective is the observation of mass ejections from the Sun by detecting large spatial scale increases in the optical surface brightness caused by Thomson scattering of sunlight upon free electrons in the interplanetary medium. This large-scale surface brightness must be measured against the much brighter (by typically 2 orders of magnitude) stellar and zodiacal-light optical field. The design photometric precision required for these solar observations allows *SMEI* to detect (at roughly 3 σ) new point sources equivalent to $V = 10$ mag.

This paper reports upper limits for optical emission at the locations of 58 out of 91 GRBs detected since *SMEI* began normal operations in early 2003 February, through a cutoff for the present work of 2005 April 6. We employ a one-orbit time window extending from 51 minutes before each burst until 51 minutes after. The particular full-sky map viewing the GRB location at the time within this window thus includes the photometric measurement of that location, at the closest time available from *SMEI*. We then compare this measurement with similar ones from one orbit earlier and one orbit later.

These 10 mag upper limits from *SMEI* are not particularly deep but are nonetheless relevant. The optical emission detected from GRB 990123 peaked at $V = 8.9$, and a number of bursts had afterglow emission brighter than 15 mag, although most bursts had much fainter upper limits, both in the observed magnitude and when scaled to the burst intensity. For most of the time period covered in this paper, there were few operating optical telescopes that observed burst locations within minutes. Even with *Swift* now being operational, *SMEI* may sometimes provide an earliest optical observation because the UVOT may not be able to reach the burst location immediately, *Swift* may not be able to relay the information to the ground (e.g., the Tracking and Data Relay Satellite System link may be disrupted), and ground-based optical telescopes may not be able to observe because of proximity to the Sun or poor weather. In addition, when the timing is fortunate, *SMEI* may cover the GRB sky location in the minutes before the observation of the burst. Thus, *SMEI* can continue to provide relevant observations.

Sections 2 and 3 describe *SMEI*, the nature of its data, and its analysis. Section 4 presents results, and the final section presents a conclusion and discussion.

2. *SOLAR MASS EJECTION IMAGER*

SMEI is designed to detect and forecast the arrival at Earth of solar mass ejections and other heliospheric structures present in the inner heliosphere. *SMEI* is mounted on the *Coriolis* spacecraft as shown in Figure 1. Each camera views the sky through a stray-light–reducing baffle and subsequent all-reflecting optics. For more details about the instrument, see Eyles et al. (2003), and about the *SMEI* mission see Jackson et al. (2004). The aperture area is 1.76 cm^2 and the bandpass that of a wide-open CCD detector, thus corresponding roughly to the "*R*" photometric band, but having a bandwidth twice as wide. A 10 mag G-type star viewed on-axis produces approximately 800 photoelectrons during a single 4 s exposure. A sidereal location near the orbital plane (roughly over the Earth's terminator) remains within the unvignetted FOV for about 1 minute each 102 minutes, while regions closer to the orbit's poles (toward the solar and antisolar directions) are observed for longer.

3. *SMEI* DATA AND ITS ANALYSIS

Figure 2 shows a typical *SMEI* data frame, a single 4 s exposure starting at 13:04:47 UT on 2004 March 23 from camera 2. A GRB was observed by *INTEGRAL* (Mereghetti et al. 2004) at the indicated location just 1 minute earlier. This event has the closest match between burst time and *SMEI* observation, of the burst locations studied in this paper. The brightness unit here is an analog-to-digital unit (ADU), one of which on the CCD is 4.7 electrons detected by a single pixel, which in turn on average covers a $0\overset{\circ}{.}05 \times 0\overset{\circ}{.}05$ patch on the sky (Eyles et al. 2003). This average brightness scale is retained when the CCD pixels are 4×4 (cameras 1 and 2) or 2×2 (camera 3) binned for telemetry on board the satellite. The UCSD *SMEI* data analysis further retains this average surface brightness when combining a sequence of frames to make a sky map (Jackson et al. 2004). The data analysis also removes most (but not all) of the Earth-radiation-band individual-pixel particle hits on the CCD, some of which are visible in Figure 2. Figure 3 presents a sky map using a sequence that spans a generous time window around the individual frame of Figure 2. Calibration analysis is presently underway at UCSD, using hundreds of stars brighter than about 4.5 mag, to establish a definitive relationship between the ADU scale on maps such as Figure 3, and an "S10," which is the equivalent surface brightness of a 10 mag G-type star, spread over a $1^\circ \times 1^\circ$ sky bin. The present value is 1 S10 = 0.4 ADU, somewhat smaller than the preliminary 0.55 value of Figure 8 in Jackson et al. (2004).

SMEI suffered a data handling unit reset about a half-hour after the data sequence shown in Figure 3, which was not remedied until about 10 hr later, so this particular GRB sky location is covered only up to the orbit shown in Figure 3. As expected, the one-orbit-earlier equivalent map to Figure 3 is nearly identical. Figure 4 is the difference map between these two, and it shows no visible-light evidence of a burst at this location. The next section summarizes this result quantitatively and presents the results of similar analyses for the other GRB events covered in the present work.

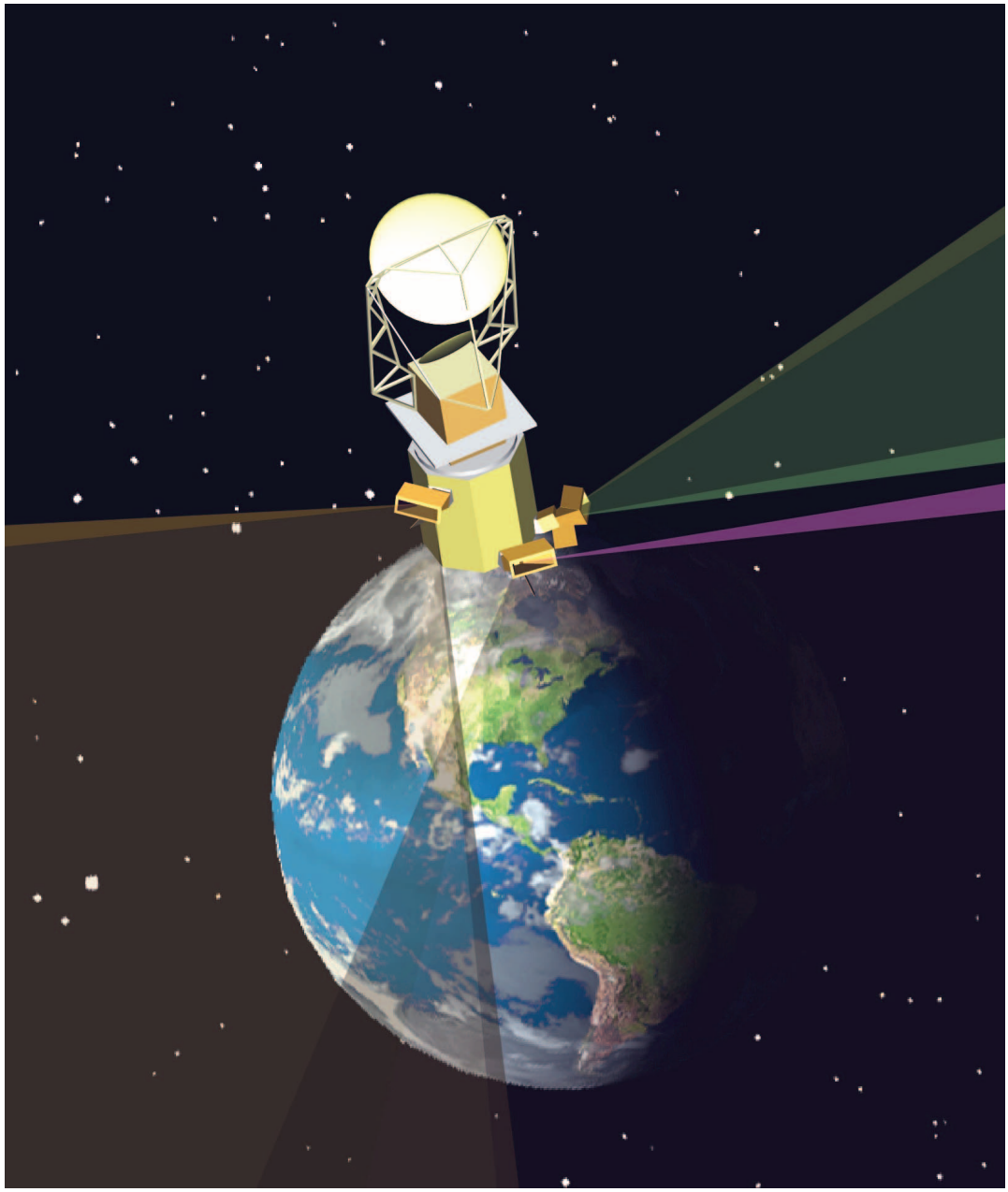

FIG. 1.—Schematic of *SMEI* as deployed in orbit on the *Coriolis* spacecraft, having just reached its northernmost position, after traveling north above the dusk terminator. The orbit is nearly circular at 840 km above the surface of the Earth and has an inclination of 98° relative to the equatorial plane. The spacecraft is zenith-pointing and oriented, as shown, with always the same side toward the Sun. *SMEI* looks outward over approximately a 160° range of sky using three strongly-baffled cameras. Their FOVs, depicted above as colored viewing columns, are oriented approximately 30° above the local horizontal to avoid both light from the Earth and sunlight from the rotating Windsat antenna, the other instrument on board this satellite. Each camera has a $3^\circ \times 60^\circ$ FOV: together these sweep out nearly the entire sky beyond about 18° from the Sun. In this article, the *SMEI* cameras are numbered from 1, viewing farthest from the Sun, to 3, viewing closest to the Sun.

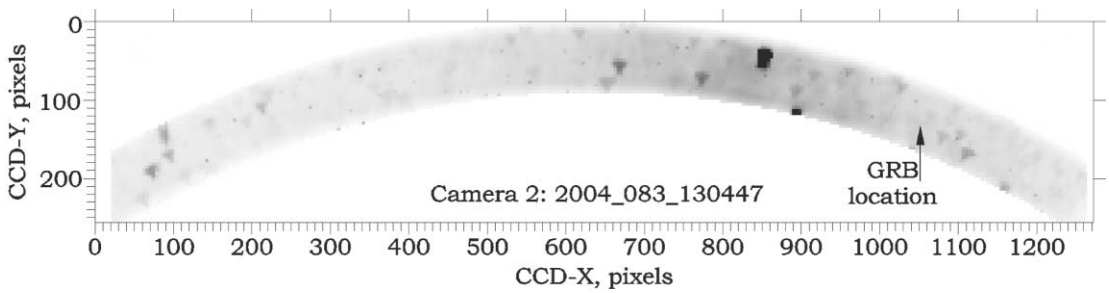

FIG. 2.—Data frame from *SMEI* camera 2 recorded on 2004 March 23, at 13:04:47 UT. The CCD pixel size labeling the axes here is about $0\overset{\circ}{.}05 \times 0\overset{\circ}{.}05$ on the sky, but these pixels were 4×4 binned on board the satellite to reduce the amount of telemetry. Contrast has been enhanced so that the range between white and black here represents a span of 1000 ADU instead of the full dynamic range of ~65,000. An electronic pedestal offset and dark current have been removed. The time is 108 s after *INTEGRAL*'s observation of GRB 040323: in this time *SMEI* moved to center the GRB sky location in the FOV narrow dimension. In a sequence of frames, stars travel across the FOV approximately radially along the narrow dimension. Sky viewed here extends from [R.A., decl.] = $[21^{\rm h}30^{\rm m}, -65^\circ]$ at the left of this frame, to $[13^{\rm h}40^{\rm m}, -43^\circ]$ at the right. The optical design bends a straight line on the sky into the above arc. The star α Cen is here located in the middle of the dark Milky Way band, just to center right above; having a peak intensity of 12,000 ADU, this star is greatly saturated with this contrast enhancement. The arrow marks the expected GRB location. Just to the right of this is the triangular group formed by M Cen (closest, about 5 mag), V774, and (farthest) a combination of four stars including SAO 241177. *SMEI*'s triangular-shaped point-spread function is evident here, as is a population of scattered particle hits on the CCD, from Earth radiation bands.

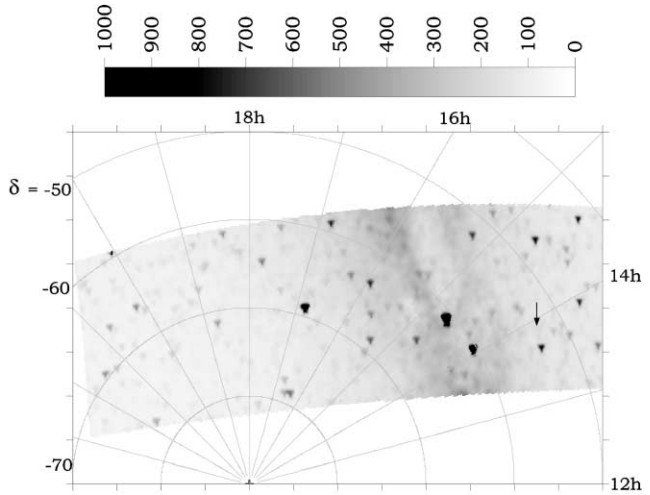

FIG. 3.—Combined average of 82 *SMEI* data frames from 13:01:03 to 13:06:27 UT on 2004 March 23. The scale here and in the next two figures is ADUs of sky surface brightness, where the original data frame brightness scale (ADU per [0.°05 × 0.°05] CCD pixel) is retained (see text). The equivalent surface brightness of a 10 mag star here is about 0.4 ADU. The coordinate frame is right ascension (hours; *right and top axes*) and declination (degrees; *left axis*). The arrow marks the sky location of the GRB.

We considered a list of 91 classical bursts (i.e., we excluded soft gamma-ray repeaters) that were detected between 2003 February 6, when *SMEI* began regular operations, and 2005 April 6. This list was selected from J. Greiner's burst compilation,[4] with a few additional bursts from the *High Energy Transient Explorer II* (*HETE II*)[5] and *Swift*[6] burst databases; data describing these bursts were extracted from all three databases. Of these, *SMEI* did not take data during nine, was in calibration mode for 22, and had data ruined by South Atlantic Anomaly particle CCD hits for two. This leaves 58 surviving candidates whose sky locations were covered within $\pm\frac{1}{2}$ orbit (51 minutes) by *SMEI*. Table 1 lists these bursts along with the burst time, the location and fluence, and the detecting mission. Fluences are not available for the bursts observed by *INTEGRAL* and the Interplanetary Network (IPN), as well as for some faint bursts detected by *HETE II* and *Swift*.

Orbit-to-orbit difference maps like Figure 4 are formed for each candidate. The selection of *SMEI* data frames is chosen generously (i.e., for about triple the time duration that the GRB location remains within the FOV) to cover the region of sky containing the GRB, for the orbit nearest in time to the burst, and the orbits immediately preceding and following it. Data are then combined within $1^\circ \times 1^\circ$ sky bins, one centered upon the expected

[4] See http://www.mpe.mpg.de/~jcg/grbgen.html.
[5] See http://space.mit.edu/HETE/Bursts.
[6] See http://swift.gsfc.nasa.gov.

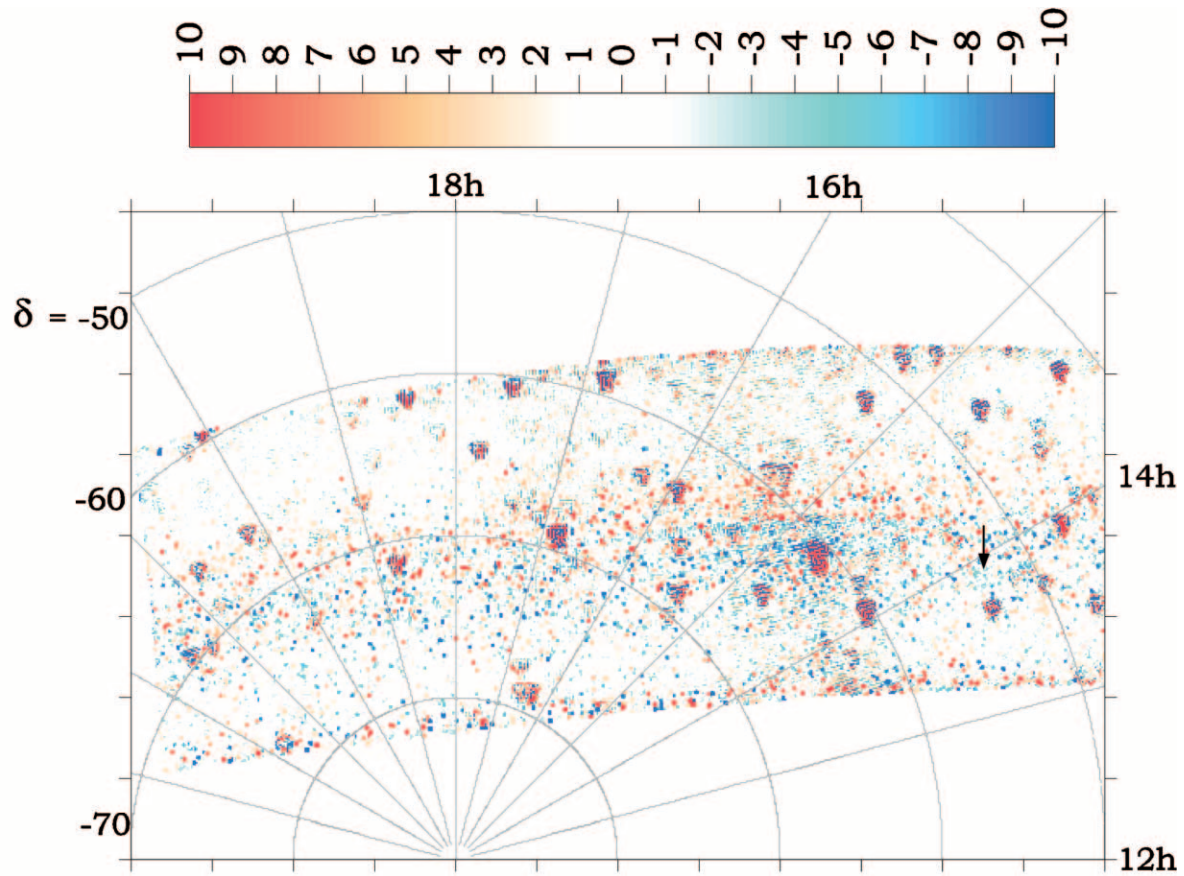

FIG. 4.—Sky map shown in Fig. 3 minus the equivalent map for the immediately previous orbit. The difference intensity scale (ADU) is 100 times enhanced compared with that of Fig. 3. As expected, the subtraction becomes noisy near bright stars. Away from these, a majority of difference bins are smaller than ±1 ADU. A residue of auroral-band particle contamination, and perhaps even some auroral light on the CCD can be seen as the red (*above*) and blue (*below*) bands that run roughly horizontally across the middle of this figure. The arrow, as in Fig. 3, marks the location of the GRB. The slight preponderance of blue (negative values) here indicates that no increase of light is observed at this location immediately after the burst.

TABLE 1

GAMMA-RAY BURST LOCATIONS THAT WERE ALSO OBSERVED BY *SMEI* WITHIN $\pm\frac{1}{2}$ ORBIT

GRB (1)	Time (UT) (2)	R.A. (J2000.0) (3)	Decl. (J2000.0) (4)	ΔPosition[a] (arcmin) (5)	Mission (6)	Fluence[b] (7)
030320	10 11 40	17 51 31	−25 18	5	*INTEGRAL*	...
030324	03 12 43	13 37 11	−00 19	7	*HETE*	$12.75^{+3.35}_{-3.01}$
030325	14 15 10	04 43:07	−19 06	60 × 4	IPN	...
030326	10 43 41	19 31 52	−11 43	65 × 3	IPN	...
030328	11 20 58	12 10 46	−09 22	2	*HETE*	$287.4^{+13.9}_{-14.1}$
030329	11 37 15	10 44 50	+21 31	2	*HETE*	$1076^{+13.0}_{-14.0}$
030418	09 59 19	10 54 53	−06 59	14	*HETE*	$17.34^{+7.27}_{-5.22}$
030429	10 42 23	12 13 06	−20 56	2	*HETE*	$3.80^{+1.40}_{-1.17}$
030519	14 04 54	16 04 36	−33 28	17 × 2	*HETE*	609.0 ± 9.7
030528	13 03 03	17 04:02	−22 39	2	*HETE*	$56.34^{+7.13}_{-7.32}$
030723	06 28 17	21 49 30	−27 42	2	*HETE*	$0.38^{+5.56}_{-0.33}$
030725	11 46 25	20 33 47	−50 46	28	*HETE*	$166.7^{+10.3}_{-10.1}$
030821	05:31 36	21 42 33	−45 12	120 × 10	*HETE*	$27.47^{+3.35}_{-2.99}$
030823	08 52 41	21 30 47	+21 59	6	*HETE*	$12.74^{+4.43}_{-3.53}$
030824	16 47 35	00 05 02	+19 55	11	*HETE*	$5.83^{+2.38}_{-1.89}$
030913	17 06 58	20 58 02	−02 12	30	*HETE*	$8.04^{+2.69}_{-1.93}$
031026	05 35 43	03 18 42	+28 22	15	*HETE*	28
031203	22 01 28	08 02 30	−39 51	2.5	*INTEGRAL*	...
031220	03 29 57	04 39 34	+07 22	11	*HETE*	4
040106	17 55 12	11 52 15	−46 46	3	*INTEGRAL*	...
040323	13 02 59	13 53 53	−52 21	2	*INTEGRAL*	...
040403	05 08 08	07 40 55	+68 13	2.7	*INTEGRAL*	...
040425	16 25 10	15 31 36	−39 43	3 × 420	*HETE*	159
040511	13 01 46	14 47 50	−44 15′	1.3	*HETE*	320
040624	08 21 35	13 00 10	−03 35	3	*INTEGRAL*	...
040701	13 00 55	20 47 46	−40 14	8	*HETE*	...
040709	00 58 08	20 53 53	−28 13	95	*HETE*	...
040730	02 11 55	15 53 16	−56 27	2	*INTEGRAL*	...
040810	14 15 36	23 54 08	−35 04	30	*HETE*	350
040812	06 01 50	16 26 05	−44 43	2	*INTEGRAL*	...
040825A	03 30 30	22 58 59	−10 56	7	*HETE*	...
040825B	16:21 37	22 46 34	−02 24	9	*HETE*	...
040903	18 17 55	18 03 22	−25 15	2.5	*INTEGRAL*	...
040912	14 12 17	23 56 54	−01 00	7	*HETE*	23
040916	00 03 30	23 01 30	−05 35	17	*HETE*	7.7
040924	11 52 11	02 06 19	+16 01	6	*HETE*	94
041006	12 18 08	00 54 53	+01 12	5	*HETE*	290
041217	07 28 30	10 59 10	−17 57	12	*Swift*	65.7
041218	15 45 25	01 39 06	+71 20	2.5	*INTEGRAL*	...
041219A	01 42 18	00 24 26	+62 50	2	*INTEGRAL/Swift*	1000
041219B	15 38 48	11 10 42	−33 27	12	*Swift*	...
041224	20 20 57	03 44 48	−06 39	7	*Swift*	125 ± 6
041226	20 34 19	05 18 10	+73 21	6	*Swift*	5.87 ± 2.71
041228	10 49 13	22:26 34	+05 03	5	*Swift*	51.4 ± 3.4
050117A	12 52 36	23 53 42	+65 56	4	*Swift*	156 ± 6
050117B	20 03 35	16 13 31	−70 21	10	*Swift*	...
050123	10 22 53	10 31 34	−11 34	14	*HETE*	31
050124	11 30 03	12:51 31	+13 02	6	*Swift*	20.0 ± 1.4
050128	04 20 04	14 38 21	−34 46	3	*Swift*	85.0 ± 5.3
050129	20 03 03	16 51 12	−03 05	3	*INTEGRAL*	...
050219A	12 40 01	11 05 38	−40 41	4	*Swift*	76.9 ± 4.0
050219B	21 05 51	05 25 06	−57 46	4	*Swift*	222 ± 10
050306	03 33 12	18 49 17	−09 10	4	*Swift*	184 ± 10
050315	20 59 43	20 25 53	−42 35	4	*Swift*	33.9 ± 2.1
050318	15 44 37	03 18 43	−46 24	4	*Swift*	16.5 ± 1.2
050319	09 31 18	10 16 38	+43 34	6	*Swift*	6.37 ± 0.92
050326	09 53 56	00 27 26	−71 22	4	*Swift*	178 ± 6
050401	14 20 15	16 31 31	+02 11	6	*Swift*	134 ± 8

NOTE.—Units of right ascension are hours, minutes, and seconds, and units of declination are degrees and arcminutes.

[a] The uncertainty in the position, usually the 90% confidence radius.

[b] Burst energy fluence F in units of 10^{-7} ergs cm^{-2}. The *HETE II* fluences are for the 30–400 keV band, while the *Swift* fluences are for the 25–350 keV band. *HETE II* fluences until GRB 030913 are taken from Sakamoto et al. (2005). Subsequent *HETE II* bursts are from pipeline processing reported on the *HETE II* World Wide Web site (http://space.mit.edu/HETE/Bursts) and were recalculated for the 30–400 keV band using spectral fits also reported there. The *Swift* fluences result from pipeline processing. No fluences are available for the bursts detected by *INTEGRAL* and the IPN, and for some faint *HETE II* and *Swift* bursts.

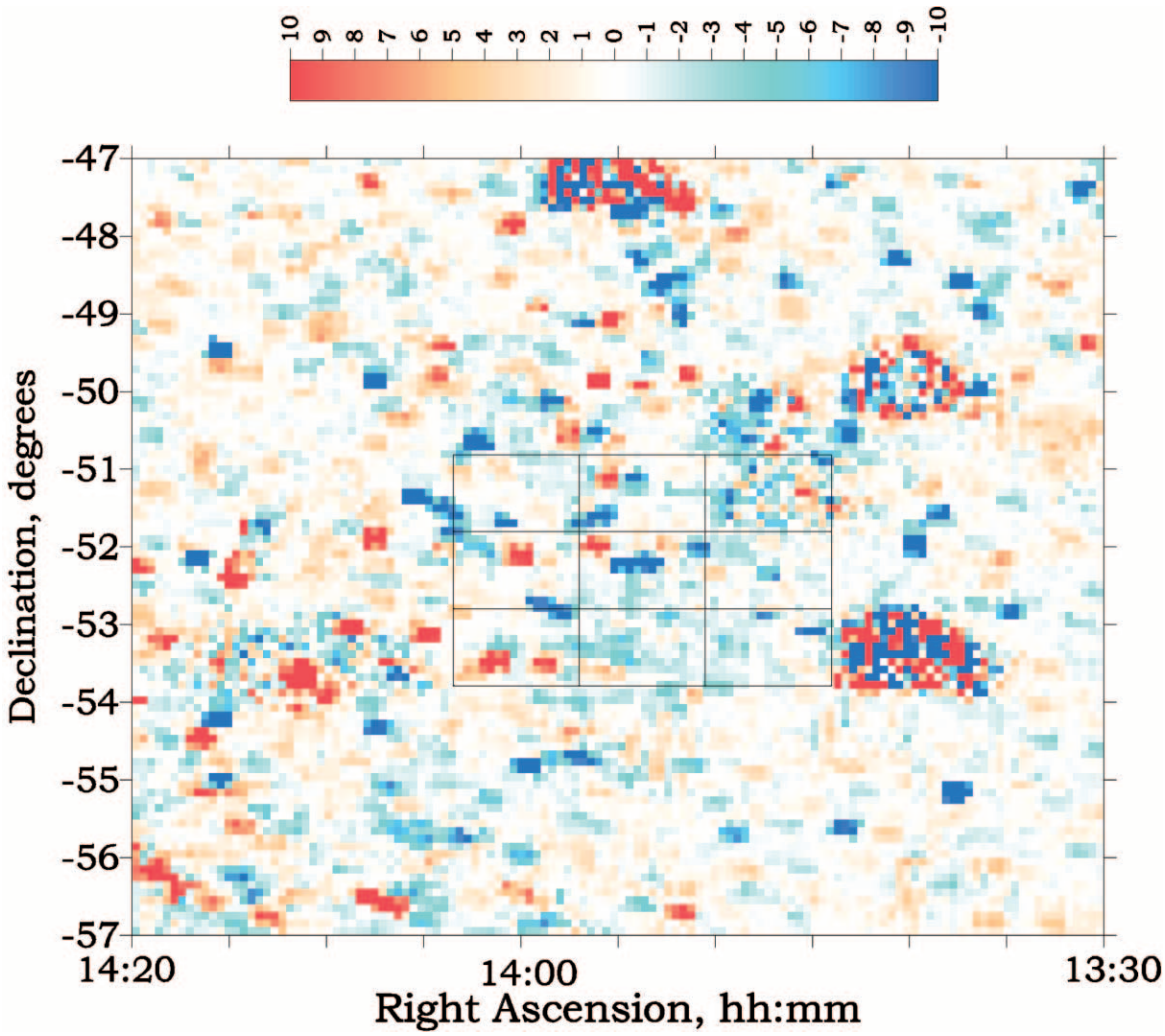

FIG. 5.—Portion of Fig. 4 near the GRB enlarged and with coordinates converted to right ascension and declination. Also shown are the nine sky bins described in the text which are used to evaluate the presence or absence of an optical counterpart to the GRB. At this enlargement, an optical counterpart would show as a red region occupying (and mostly filling) the center bin. Instead, we see smaller regions of red and blue, typical residues of particle impacts on the CCD, not entirely removed by the indexing analysis. At this enlargement also, the subtraction of individual stars such as bright ε Cen, located here just to the right of the boxes, is noisy because of photoelectron counting-statistics uncertainties within these small sky bins.

GRB location and its eight neighboring bins. This sky bin size covers the fish-shaped triangular point-spread function for *SMEI* (see § 3.1 in Eyles et al. [2003] for a more detailed description of the optics). Figure 5 shows the appropriate portion of Figure 4 enlarged and converted to right ascension and declination coordinates, and the appropriate nine bins above shown as boxes. A plane is fitted through the values of the eight neighboring bins, and then the values predicted by this plane are subtracted from the observed values in all nine bins. This process removes any potential transient difference between the maps, such as auroral light or heliospheric structures, that varies slowly with sky position.

Next, a standard deviation $\sigma = (\sigma^2)^{1/2}$ is calculated using the neighbors alone, from the following variance formula:

$$\sigma^2 = \frac{1}{5}\sum_{i=1}^{8}(R_i - R_i^p)^2. \quad (1)$$

Here R_i and R_i^p are, respectively, the differential photometric response for the eight bins and the fitted planar value, and the 5 in the denominator is the number of degrees of freedom (eight measurements minus the three parameters for the plane). This σ estimates the intrinsic noise at this sky location, under the assumption that the intrinsic noise of a given $1^\circ \times 1^\circ$ sky bin differs little from its immediate neighbors. This assumption is likely correct for additional noise such as slowly varying background light or a residue of particle hits not removed by the analysis. Some of the latter are seen in Figure 4 as isolated red and blue spots, and in Figure 5 as patchy red and blue regions smaller than the stars. On the other hand, this assumption may not be correct when a nearby bright star lies partly or wholly within the group of nine bins.

Five of these bursts have sky locations uncertain by more than 0.°5 (see col. [5] in Table 1). For these a more extensive analysis was performed to see whether relocating the analysis region at 0.°1 intervals, to cover a $2^\circ \times 2^\circ$ square centered on the nominal expected sky location, would alter the result. Photometric results for three of these were insensitive to this change in the expected location of the GRB. Two showed a photometric change, but at the nearby location of a presumably variable bright star; these thus are discounted here as GRBs. GRB 040425 received a further analysis, because its error box is $3' \times 7^\circ$ (i.e., long and narrow) in the sky: here we repeated the above, but using larger 0.°3 intervals to explore a $6^\circ \times 6^\circ$ square of sky. The photometric

TABLE 2

SMEI Measurements at Gamma-Ray Burst Locations

GRB (1)	Camera Number (2)	Δt[a] (3)	N[b] (4)	Δ_{2-1} (ADU) (5)	Δ_{3-2} (ADU) (6)	σ_{21} (7)	σ_{32} (8)	$\Delta_{2-1}/\sigma_{2-1}$ (9)	$\Delta_{3-2}/\sigma_{3-2}$ (10)	3 σ Limit m_v (mag) (11)	Comments[c] (12)
030320.....	2	+35	21	3.65	12.3	2.39	6.5	1.5	1.9	6.6	A
030324.....	1	−28	49	0.13	0.53	0.49	0.25	0.3	2.1	9.3	B
030325.....	2	+45	21	−0.83	1.62	0.81	0.44	−1.0	3.7	8.7	C
030326.....	2	−4	21	−0.14	0.06	0.05	0.24	−2.8	0.3	10.3	
	3	−7		0.48	0.17	1.98	0.33	0.2	0.5	∼9.0[d]	Orbit 1, Moon nearby
030328.....	1	+44	68	0.26	0.35	0.70	0.24	0.4	1.5	9.0	B, orbit 1
030329.....	1	+44	44	0.07	0.19	0.24	0.19	0.3	1.0	9.8	
030418.....	1	−17	28	0.01	−0.02	0.08	0.11	0.1	−0.2	10.7	
030429.....	1	+46	29	−0.30	0.21	0.60	0.40	−0.5	0.5	8.9	C
030519.....	1	−14	30	0.55	0.00	0.67	0.99	0.8	0.0	8.4	B
030528.....	1	−14	37	−1.42	−0.40	1.24	0.55	−1.1	−0.7	8.3	B, orbits 1 and 3
030723.....	1	+5	28	0.25	−0.42	0.25	0.21	1.0	−2.0	9.8	
030725.....	1	−34	24	0.92	0.09	0.84	0.95	1.1	0.1	8.3	B
	2			0.21	−0.16	1.08	0.76	0.2	−0.2	8.3	B
030821.....	1	−30	25	−0.04	−0.01	0.22	0.10	−0.2	−0.1	10.2	
030823.....	1	−26	82	0.82	−0.41	0.39	0.32	2.1	−1.3	9.3	A
030824.....	1	+19	41	−0.08	−0.14	0.09	0.09	−0.9	−1.6	10.8	
030913.....	1	+9	32	−0.13	0.01	0.06	0.11	−2.2	0.1	10.9	
031026.....	1	−17	49	1.10	−0.51	1.25	0.53	0.9	−1.0	8.3	C, D, orbit 1
031203.....	2	−11	22	4.2	...	0.80	...	5.3	...	8.0	B, C
031220.....	1	+18	70	0.10	−0.33	0.10	0.11	1.0	−3.0	10.6	
040106.....	2	+41	20	−0.17	−0.81	0.47	1.93	−0.4	−0.4	8.0	A, orbit 3; B, orbit 2
040323.....	2	+1	21	−0.47	...	0.54	...	−0.9	...	8.5	B
040403.....	2	+27	20	−0.53	−0.13	0.27	0.17	−2.0	−0.8	9.8	
040425.....	1	−34	24	0.70	−0.66	1.46	0.33	0.5	−2.0	∼9.0[d]	B
040511.....	1	+36	25	−0.33	−0.03	0.22	0.18	−1.5	−0.2	9.9	
040624.....	2	−5	21	−0.15	−0.37	0.09	0.27	−1.7	−1.4	10.0	
040701.....	1	−34	24	...	−0.07	...	0.56	...	−0.1	8.4	A
040709.....	1	+36	29	−0.13	−0.17	0.46	0.96	−0.3	−0.2	8.5	C
040730.....	2	+18	24	0.85	−1.24	1.40	1.22	0.6	−1.0	7.9	Crowded galactic center
040810.....	1	+3	24	−0.22	0.05	0.24	0.14	−0.9	0.4	10.0	
	2	+4		0.03	0.34	0.97	0.20	0.0	1.7	∼9.5[d]	A, orbit 1; B, orbit 2
040812.....	2	−29	20	−0.83	...	0.74	...	−1.1	...	8.1	B
040825A.....	1	−29	54	−0.61	−0.10	0.41	0.64	−1.5	−0.2	8.9	D
040825B.....	1	+3	74	0.02	...	0.15	...	0.1	...	9.9	
040903.....	2	+31	21	−1.61	...	0.79	...	−2.0	...	8.1	B
040912.....	1	+16	104	−0.11	0.33	0.19	0.16	−0.6	2.1	10.1	
040916.....	1	+6	74	−1.39	0.42	3.27	0.67	−0.4	0.6	∼8.2[d]	A, orbit 1; B, orbit 2
040924.....	1	+34	42	−2.98	0.02	0.79	0.10	−3.8	0.2	∼10.3[d]	A, orbit 1
041006.....	1	+19	143	−0.93	−0.45	0.45	0.94	−2.1	−0.5	8.6	B, orbit 1; bad quaternions,[e] orbit 3
041217.....	2	+49	20	2.32	−3.13	1.76	2.40	1.3	−1.3	7.4	A
041218.....	2	+7	21	1.21	−0.96	0.66	0.60	1.8	−1.6	8.7	B
041219A.....	2	+16	21	−0.78	0.25	0.68	0.55	−1.1	0.5	8.7	C
041219B.....	2	+36	20	−0.29	0.25	0.36	0.42	−0.8	0.6	9.2	D
041224.....	1	+3	31	0.01	−0.06	0.18	0.08	0.1	−0.8	10.4	
041226.....	2	−22	22	0.41	0.04	0.46	0.14	0.9	0.3	9.5	B, orbit 1
041228.....	3	+8	25	−1.02	0.55	1.16	1.19	−0.9	0.5	8.0	
050117A.....	2	+47	20	−4.6	6.6	5.0	7.6	−0.9	0.9	6.2	A, all three orbits
050117B.....	2	+40	22	4.5	0.30	3.05	7.0	1.5	0.0	6.4	A all three orbits
050123.....	1	+36	30	−0.01	1.99	3.44	2.07	0.0	1.0	7.1	A, all three orbits
050124.....	2	+43	22	−0.04	0.23	0.24	0.20	−0.2	1.2	9.8	
050128.....	2	+7	21	0.16	0.10	0.23	0.43	0.7	0.2	9.4	C
050129.....	3	+48	33	1.43	−3.34	6.2	6.2	0.2	−0.5	6.2	
050219A.....	1	+37	26	−0.78	1.92	1.19	1.78	−0.7	1.1	7.7	A, all three orbits
050219B.....	2	+40	16	−1.80	−0.40	2.57	3.68	−0.7	−0.1	6.9	A, all three orbits
050306.....	3	+3	20	0.25	−1.76	2.42	2.32	0.1	−0.8	7.2	
050315.....	3	+27	25	−0.61	−1.12	2.39	1.94	−0.3	−0.6	7.3	
050318.....	3	+9	26	−2.04	−0.02	0.84	0.88	−2.4	0.0	8.3	
050319.....	1	−9	32	0.44	...	0.91	...	0.5	...	7.9	C
050326.....	3	+5	25	−1.77	0.06	1.82	0.80	−1.0	0.1	7.9	
050401.....	1	+13	24	−0.14	0.08	0.37	0.29	−0.4	0.3	9.4	C
	2			−0.18	0.44	0.20	0.33	−0.9	1.3	9.6	C

[a] The least time in minutes between the burst and a *SMEI* window of observation for that location.

[b] The number of 4 s *SMEI* exposures during which the GRB location remains within that camera's FOV for one orbit.

[c] Letters in the comments column indicate the following: A = substantial particle contamination from SAA or auroral ovals; B = modest particle contamination from SAA or auroral ovals; C = nearby bright star partly within neighboring sky bins; and D = nearby space debris.

[d] Only one σ was used.

[e] Flawed spacecraft pointing information.

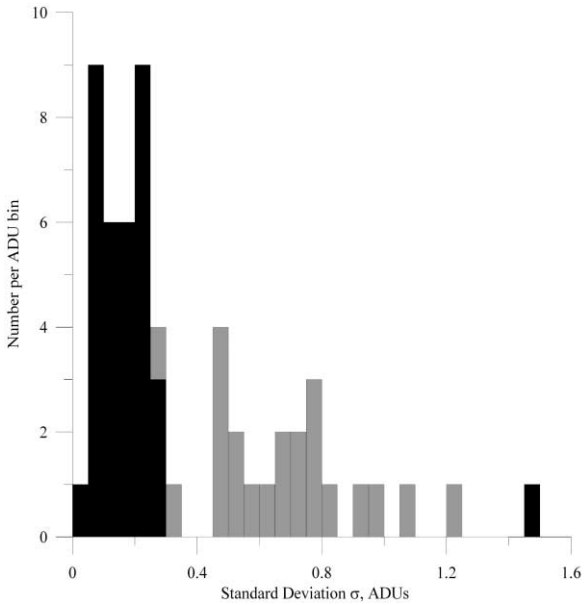

FIG. 6.—Histogram of σ values for cameras 1 and 2 from Table 2, both those free of noise-increasing background (*black*) and having modest residual particle contamination (*gray*), as indicated by comment B.

result remained essentially unchanged, except at several bright-star locations contained within this larger area.

4. RESULTS

Table 1 lists the 58 GRBs and summarizes their properties. Table 2 provides the *SMEI* results for the same 58 bursts. Columns (5) and (6), respectively, provide the differences between the closest-in-time *SMEI* measurement and the one-orbit-earlier and one-orbit-later *SMEI* measurements, and columns (7) and (8) the neighbors-defined standard deviation. Columns (9) and (10), respectively, provide the ratios of column (5) to (7) and (6) to (8) (i.e., the signal-to-noise ratio, hence a measure of the statistical significance of the measurement). Briefly, no optical counterparts are observed greater than 5.3 σ for any of the bursts.

In Table 2, note that when Δt is positive, *SMEI* looks at that particular place in the sky *after* the GRB time and thus an optical counterpart would be indicated by a positive value in the Δ_{2-1} column. When Δt is negative, *SMEI* looks earlier, so a positive value in the Δ_{2-1} column would indicate that an optical counterpart had occurred *before* the indicated GRB time. If such optical counterpart were to fade quickly, this would be followed by a comparable negative value in the Δ_{3-2} column. On the other hand, if when Δt is negative an optical counterpart were to be present only in the third orbit, we would expect then to see a small or zero value in the Δ_{2-1} column, and instead a positive value in the Δ_{3-2} column.

We chose in Figures 2–5 to highlight the GRB of 2004 March 23, simply because it had the smallest Δt. As indicated by the blue patch in the middle bin of Figure 5, this region of sky yields in Table 2 a slightly negative value (-0.47) for the brightness of a potential optical counterpart, which lies well within the indicated range of measurement ($\sigma = 0.54$) determined by the eight neighboring bins.

SMEI was designed to provide 0.1% differential photometry in a $1^\circ \times 1^\circ$ sky bin, including photoelectron counting statistical fluctuations, subpixel gradients, flat-field-correction errors, and star registration error. Here typical sky brightnesses are 100 ADU (e.g., see Fig. 3), so 0.1% performance should yield a typical σ in Table 2 of $\sqrt{2} \times 0.1 = 0.14$ ADU, where the $\sqrt{2}$ factor accounts the difference between two sky maps. Some σ values are likely augmented by residual contamination from radiation-band particles, possibly some direct auroral light, and in some cases by the partial inclusion of nearby bright stars. In our example, star M Cen lies in the top right box of Figure 5. The "comments" column of Table 2 indicates which *SMEI* data for GRBs are seen to suffer from particle contamination and other noise-increasing phenomena. GRB 030325 and GRB 031203 have photometric deviations greater than 3 σ, but these both suffer from presumably variable bright stars within the analysis region. Finally, GRB 040924 is similarly discounted since it has significant particle contamination and also the wrong sign for a legitimate GRB when Δt is positive.

Figure 6 presents a histogram of camera 1 and 2 σ values from Table 2, both for data having no comment and with only modest particle contamination (comment B in the table). Camera 3 is here excluded because it has a significantly higher noise level than the others. When the data are clean, *SMEI*'s photometric performance with this type of orbit-to-orbit-difference analysis is close to the original 0.1% design specification, here corresponding to $\sqrt{2}/1000$ of sky surface brightnesses that here range from 50 to 200 ADU. With modest contamination, σ values become somewhat larger (shaded portion of the histogram). Typically 30% of the individual orbits do have a "noticeable" particle contamination or worse, and therefore about half of the rows in Table 2 are flagged. Modest contamination residue increases σ by two- to three-fold, but larger contamination or interference by nearby bright stars or space debris can increase σ dramatically.

Column (11) of Table 2 presents a 3 σ upper limit for m_v, using the preliminary estimate of one S10 = 0.4 ADU and an overall measurement standard deviation of $(\sigma_{2-1} + \sigma_{3-2})/(2\sqrt{2})$ when both differences are present, otherwise the appropriate single σ value from the table. In five cases when one σ is much smaller than the other, the small σ was used by itself and the approximate upper limit is indicated. Conversion of this m_v to an m_r as is more usual in this context, requires an assumed spectrum shape for the alleged GRB. When the spectrum follows frequency $\nu \propto \nu^{-1}$, then the *SMEI* limit for m_r is about 0.25 mag fainter than the m_v given in Table 2, whereas if $\nu \propto \nu^{-2}$, then the *SMEI* limit for m_r is about 0.5 mag fainter.

5. DISCUSSION

For the study of gamma-ray afterglows, our primary result is the set of upper limits at different times Δt relative to the burst

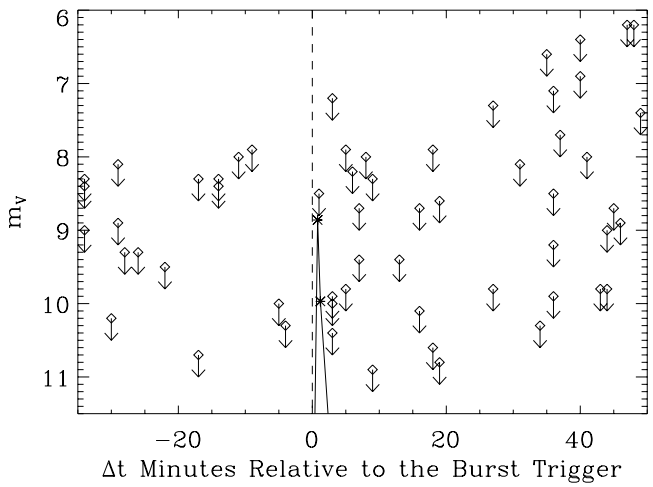

FIG. 7.—*SMEI* 3 σ upper limits for m_v vs. Δt (time relative to the burst), from Table 2. The points with asterisks connected by solid lines are the GRB 990123 observations (Akerlof et al. 1999).

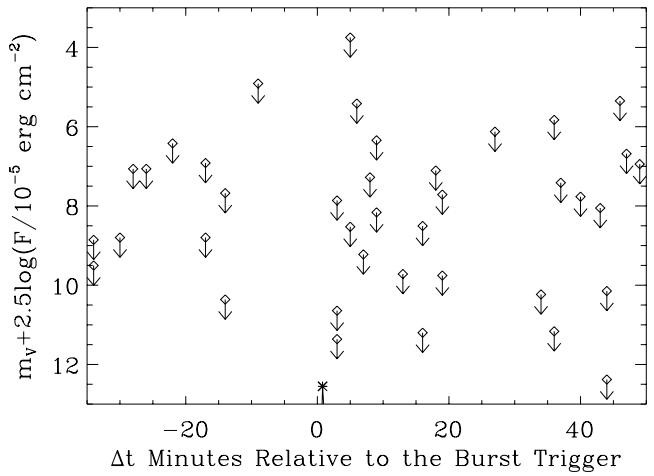

FIG. 8.—*SMEI* 3 σ upper limits for m_v normalized by the fluence F in units of 10^{-5} ergs cm^{-2} (i.e., $m_v + 2.5 \log [F/10^{-5}$ ergs cm^{-2}]) vs. Δt. The point with an asterisk near $\Delta t = 0$ is the GRB 990123 observation (Akerlof et al. 1999).

presented in Table 2. Figure 7 shows this result graphically. Assuming that the intensity of the afterglow and the burst are correlated, we show in Figure 8 the ratio of the optical flux upper limit normalized by the fluence as a function of Δt for those bursts where the fluence is available. In both figures the comparable values for the GRB 990123 detection (Akerlof et al. 1999) are shown. As can be seen, the optical limits are generally not particularly deep. However, the upper limits for small Δt are comparable to the GRB 990123 detection and therefore do constrain the afterglow.

The combination of the *SMEI* upper limits and later afterglow detections constrain the temporal decay of the afterglow. We considered all bursts observed by *SMEI* within 10 minutes before or after the burst trigger. Unfortunately, no optical afterglows were detected for GRBs 030326, 040323, 040624, 040810, 040825A, 041224, 041228, 050128, 050306, and 050326. Detections or upper limits on the same timescale as, but fainter than, the *SMEI* observations were reported for GRBs 030723 (Smith et al.2003) and 050319 (Boyd et al. 2005), and therefore the *SMEI* observations are not interesting for these bursts. Table 3 presents the bursts for which there are both *SMEI* upper limits and later optical detections. Where *R*-band detections are reported, we used a color correction of 0.5 (as discussed above) to compare the upper limits and detections. The observations constrain the power-law index α, $f_\nu \propto \Delta t^{-\alpha}$. As can be seen, none of the limits on the power-law index are particularly constraining.

TABLE 3
CONSTRAINTS ON AFTERGLOW DECAY

GRB (1)	Δt[a] (2)	m_v[b] (3)	Δt[c] (4)	Detection[d] (5)	α[e] (6)	Reference[f] (7)
040916.....	6	8.2	186	22.3	<4.0	Kosugi et al. (2004)
041218.....	7	8.7	25	18.6[g]	<7.16	Trondal (2004)
			141	19.5	<3.16	Greco et al. (2004)
050318.....	9	8.4	55	18.4	<4.9	McGowan et al. (2005)

[a] Time between burst trigger and *SMEI* observation, in minutes.
[b] *SMEI* 3 σ upper limit.
[c] Time in minutes between burst trigger and optical detection.
[d] Optical detection, in m_r, unless otherwise specified.
[e] Power-law index α, $f_\nu \propto \Delta t^{-\alpha}$, of the afterglow's temporal decay.
[f] Reference for optical detection.
[g] Optical detection in *V* band.

The black parts of the histogram in Figure 6 show—in the absence of interference by Earth radiation-band particles, space debris, or variation due to nearby stars—that *SMEI* imagery is indeed differentially photometric at the design specification of 0.1%, within a $1^\circ \times 1^\circ$ sky bin. This performance was noted in Figure 8 of Jackson et al. (2004), but here extends to the wide variety of sky locations and times of these GRBs.

While the *SMEI* sensitivity cannot compare with the sensitivity of the UVOT on *Swift* or the ground-based robotic telescopes such as ROTSE-III, future *SMEI* observations are still relevant when these more sensitive telescopes are unable to observe a burst, whether because of observational constraints or because of bad weather. *SMEI* observations, whether detections or upper limits, are relevant given the optical detections of GRB 990123 and (although fainter) of GRB 041219A during the burst, afterglow detections brighter than 15 mag, and the complex X-ray afterglows observed by *Swift*'s XRT. Therefore, from time to time we will release detections and/or upper limits for the burst locations viewed by *SMEI* in the hour before or after the burst.

SMEI was designed and constructed by a team of scientists and engineers from the US Air Force Research Laboratory, the University of California at San Diego, Boston College, Boston University, and the University of Birmingham in the UK. Financial support was provided by the Air Force, the University of Birmingham, and NASA. The work at UCSD was supported in part by AFRL contract AF19628-00-C-0029, AFOSR contract AF49620-01-0054, and NASA grant NAG5-134543.

REFERENCES

Akerlof, C., et al. 1999, Nature, 398, 400
———. 2000, ApJ, 532, L25
Blake, C. H., et al. 2005, Nature, 435, 181
Boyd, P., et al. 2005, GCN 3129, http://gcn.gsfc.nasa.gov/gcn/gcn3/3129.gcn3
Briggs, M. S., et al. 1999, ApJ, 524, 82
Eyles, C. J., et al. 2003, Sol. Phys., 217, 319
Fenimore, E. E., Madras, C. D., & Nayaksin, S. 1996, ApJ, 473, 998
Gehrels, N., et al. 2004, ApJ, 611, 1005
Greco, G., Bartolini, C. Guarnieri, A., Piccioni, A., Ferrero, P., Pizzichini, G., & Gualandi, R. 2004, GCN 2863, http://gcn.gsfc.nasa.gov/gcn/gcn3/2863.gcn3
Jackson, B. V., et al. 2004, Sol. Phys., 225, 177
Kosugi, G., Kawai, N., Tajitsu, A., & Furusawa, H. 2004, GCN 2726, http://gcn.gsfc.nasa.gov/gcn/gcn3/2726.gcn3
Kulkarni, S. R., et al. 1999, ApJ, 522, L97
Li, W., Filippenko, A. V., Chornock, R., & Jha, S. 2003, ApJ, 586, L9
McGowan, K., et al. 2005, GCN 3115, http://gcn.gsfc.nasa.gov/gcn/gcn3/3115.gcn3
Mereghetti, S., et al. 2004, GCN 2551, http://gcn.gsfc.nasa.gov/gcn/gcn3/2551.gcn3
Mészáros, P., & Rees, M. J. 1997, ApJ, 476, 232
Nakar, E., & Piran, T. 2004, MNRAS, 353, 647
Nysewander, M. C., et al. 2005, ApJ, submitted (astro-ph/0505474)
Piran, T. 2005, Rev. Mod. Phys., 76, 1143
Rykoff, E. S., Yost, S. A., Rujopakarn, W., Swan, H., Alatalo, K., & Quimby, R. 2005a, GCN 3726, http://gcn.gsfc.nasa.gov/gcn/gcn3/3726.gcn3
Rykoff, E. S., Yost, S. A., & Swan, H. 2005b, GCN 3465, http://gcn.gsfc.nasa.gov/gcn/gcn3/3465.gcn3
Sakamoto, T., et al. 2005, ApJ, 629, 311
Smith, D. A., Akerlof, C. W., & Quimby, R. 2003, GCN 2338, http://gcn.gsfc.nasa.gov/gcn/gcn3/2338.gcn3
Trondal, O. 2004, GCN 2877, http://gcn.gsfc.nasa.gov/gcn/gcn3/2877.gcn3
van Paradijs, J., Kouveliotou, C., & Wijers, R. A. M. J. 2000, ARA&A, 38, 379
Vestrand, W. T., et al. 2004, Astron. Nachr, 325, 549
———. 2005, Nature, 435, 178
Williams, G., et al. 1999, ApJ, 519, L25
Yost, S. A., Swan, H., Schaefer, B. A., & Alatalo, K. 2005, GCN 3322, http://gcn.gsfc.nasa.gov/gcn/gcn3/3322.gcn3